Physica Medica 30 (2014) 133–146

Contents lists available at SciVerse ScienceDirect

Physica Medica

journal homepage: http://www.physicamedica.com

Review paper

Computational assessment of deep-seated tumor treatment capability of the $^{9}Be(d,n)^{10}B$ reaction for accelerator-based Boron Neutron Capture Therapy (AB-BNCT)

M.E. Capoulat [a,b,c,*], D.M. Minsky [a,b,c], A.J. Kreiner [a,b,c]

[a] Gerencia de Investigación y Aplicaciones, CNEA, Av. Gral. Paz 1499 (B1650KNA), San Martín, Buenos Aires, Argentina
[b] Escuela de Ciencia y Tecnología, Universidad Nacional de San Martín, M. de Irigoyen 3100 (1650), San Martín, Buenos Aires, Argentina
[c] CONICET. Av. Rivadavia 1917 (C1033AAJ), Buenos Aires, Argentina

ARTICLE INFO

Article history:
Received 30 January 2013
Received in revised form
10 June 2013
Accepted 2 July 2013
Available online 21 July 2013

Keywords:
Accelerator-based BNCT
$^{9}Be(d,n)^{10}B$ reaction
Monte-Carlo-simulations
Brain tumor treatment

ABSTRACT

The $^{9}Be(d,n)^{10}B$ reaction was studied as an epithermal neutron source for brain tumor treatment through Boron Neutron Capture Therapy (BNCT). In BNCT, neutrons are classified according to their energies as thermal (<0.5 eV), epithermal (from 0.5 eV to 10 keV) or fast (>10 keV). For deep-seated tumors epithermal neutrons are needed. Since a fraction of the neutrons produced by this reaction are quite fast (up to 5–6 MeV, even for low-bombarding energies), an efficient beam shaping design is required. This task was carried out (1) by selecting the combinations of bombarding energy and target thickness that minimize the highest-energy neutron production; and (2) by the appropriate choice of the Beam Shaping Assembly (BSA) geometry, for each of the combinations found in (1). The BSA geometry was determined as the configuration that maximized the dose deliverable to the tumor in a 1 h treatment, within the constraints imposed by the healthy tissue dose adopted tolerance. Doses were calculated through the MCNP code.

The highest dose deliverable to the tumor was found for an 8 μm target and a deuteron beam of 1.45 MeV. Tumor weighted doses ≥40 Gy can be delivered up to about 5 cm in depth, with a maximum value of 51 Gy at a depth of about 2 cm. This dose performance can be improved by relaxing the treatment time constraint and splitting the treatment into two 1-h sessions. These good treatment capabilities strengthen the prospects for a potential use of this reaction in BNCT.

Introduction

Background

Boron Neutron Capture Therapy (BNCT) [1,2] is a modality currently under development worldwide [3] for the treatment of some types of diffuse, infiltrating and/or very radioresistant malignant tumors such as high-grade gliomas of the central nervous system among others. This binary radiotherapy modality combines the selective administration of a thermal-neutron capture agent – the stable isotope ^{10}B – and the irradiation of the affected region with a high-intensity thermal neutron flux. The neutron capturer is delivered ideally via a tumor-seeking agent so that the ^{10}B uptake is enhanced in tumor cells compared to normal tissues. Then, when the target region is irradiated with thermal neutrons (<0.5 eV), an alpha particle of 1.47 MeV and a Li ion of 840 keV are produced from the capture reaction $^{10}B(n,\alpha)^{7}Li$. Since the ranges of these particles (of about 8 μm and 5 μm respectively) are comparable to the typical cell diameter, the radiation damages the target cell without harming the surrounding tissues.

The success of BNCT relies on (i) the effective and selective delivery of a sufficient quantity of boron to the targeted tumor, and (ii) a sufficient intense flux of thermal neutrons at the tumor location. For deep seated tumors, clean-epithermal (0.5 eV–10 keV) neutron beams are needed, since they thermalize on the way to the tumor and reach it with energies that maximize the capture reaction cross-section. Thermal and fast (>10 keV) contaminations to

* Corresponding author. Gerencia de Investigación y Aplicaciones, CNEA, Av. Gral. Paz 1499 (B1650KNA), San Martín, Buenos Aires, Argentina. Tel.: +54 11 6772 7067; fax: +54 11 6772 7121.
E-mail address: capoulat@tandar.cnea.gov.ar (M.E. Capoulat).

1120-1797/$ – see front matter © 2013 Associazione Italiana di Fisica Medica. Published by Elsevier Ltd. All rights reserved.
http://dx.doi.org/10.1016/j.ejmp.2013.07.001

the epithermal neutron beam produce undesirable effects. Thermal neutrons have a limited penetration depth, not being suitable for deep seated tumor treatments. On the other hand, fast neutrons produce high LET recoil protons, primarily by scattering on hydrogen present in tissues, which in turn deliver undesirable dose to the healthy tissues.

Early BNCT clinical trials failed to achieve either of these goals [4,5]. Concerning the boron delivery, the development of a suitable tumor-seeking agent is an ongoing and highly complex task of high priority. Only two boron-containing compounds are still being used in clinical trials. These are sodium borocaptate [6] ($Na_2B_{12}H_{11}SH$), (known as BSH) and boronophenylalanine [7] (or BPA). Concerning the neutron beam design, the implementation of epithermal columns in reactor facilities improved significantly the neutron beam quality [8,9]. Very good neutron beam qualities have been achieved and used clinically with an important degree of success [10–18].

Accelerator-based BNCT

So far, BNCT clinical trials have been carried out in nuclear reactor facilities. However, Accelerator-based (AB) neutron sources have been a matter of interest for almost 30 years [19–25], because of their much lower cost and level of complexity compared to a reactor-based facility, and mainly because they permit in-hospital siting. Some nuclear reactions were proposed as a possible neutron source for AB-BNCT [25–28]. Among them, the ^{7}Li(p,n)^{7}Be reaction is probably the optimal from a neutronic point of view since it provides relatively low-energy neutrons with a significant cross-section. Computational dose assessment of such a facility showed good treatment performances both for superficial and deep-seated tumors [29]. However, the implementation of a metallic Li-based target constitutes a non-trivial challenge from a technological point of view. First, the low melting point (180 °C) and thermal conductivity (84.7 W/m-K) make it difficult to keep the target in solid state. On the other hand, the ^{7}Be, 53 day radioactivity produced by the ^{7}Li(p,n) ^{7}Be reaction is a non-negligible complication to deal with. In order to partially reduce the complexity of the target cooling systems, liquid-Li targets have been proposed as an alternative. Such prototypes are under development at the Soreq Nuclear Research Center (SNRC) in Israel [30] and at the Kyoto University Research Reactor Institute (KURRI) in Japan [31]. To handle the complications derived from the residual radioactivity, cold Be traps are also under development. In particular, for liquid-Li targets, this becomes more important due to the eventual evaporation of the residual ^{7}Be.

In this context, the use of beryllium targets may constitute an advantage concerning target engineering design. Metallic Be has more suitable thermal and mechanical properties (the melting point and thermal conductivity of Be are 1287 °C and 190 W/m-K, respectively as compared to 180 °C and 84.7 W/m-k for metallic Li). This fact certainly allows avoiding most of the difficulties related to cooling requirements of a lithium-based target.

The closest to a clinical accelerator-based neutron source is the Cyclotron-Based Epithermal Neutron Source (C-BENS) at the Kyoto University Research Reactor Institute (KURRI) in Japan [32]. This facility produces neutrons through the ^{9}Be(p,n)^{9}B reaction, using a 1 mA beam of protons of 30 MeV. However, the high energy of the neutrons produced (up to 28 MeV) constitutes a disadvantage concerning the exposure and the subsequent activation of the surrounding materials [33]. Also in Japan, another ^{9}Be(p,n)-based accelerator facility is being constructed at the Ibaraki-prefecture [34]. In this case, the accelerator is a combination of an 8 MeV (10 mA) proton Linac consisting of a radiofrequency quadrupole and a Drift Tube Linac (DTL).

Another possible source of neutrons is the ^{9}Be(d,n)^{10}B reaction. Mc Michael et al. [35] first studied this reaction for BNCT. This study is focused on the evaluation of different reactions as a therapeutic neutron source. It evaluates the achievable epithermal flux and the fast neutron contamination for a thick Be target bombarded by a 20 mA beam of 2.6 MeV deuterons. The authors discard this neutron source because of the amount of fast neutron contamination. However, the use of a thin target allows reducing most of the fast neutron contribution to the neutron spectrum, and hence, to improve the prospects for a potential use of this reaction in BNCT. Colonna et al. [36] had already stated the possibility of reducing the fast neutron contamination by using a thin target.

In Argentina, a Tandem-ElectroStatic Quadrupole (TESQ) accelerator is under construction at the National Atomic Energy Commission [37]. In a first stage of development, the machine is intended to deliver a high intensity beam of deuterons of about 1.4 MeV, to work in conjunction with a thin Be target. In this context a thorough study on the potential use of the ^{9}Be(d,n)^{10}B as an epithermal neutron source is presented here.

^{9}Be(d,n)^{10}B-Based neutron sources

The ^{9}Be(d,n)^{10}B reaction is exothermic (Q = 4.36 MeV), and consequently produces fast neutrons. In the low-bombarding energy regime (<1.5 MeV) the neutron spectra extend to 5–6 MeV. However, when the target is bombarded with deuterons near and above 1 MeV, three closely spaced excited levels in the residual ^{10}B nucleus (designated N6, N7 and N8 at 5.11, 5.16 and 5.18 MeV respectively [38]) are preferentially populated as they become energetically accessible (Fig. 1). Therefore, most of the energy released in the reaction (which is near and above 5 MeV) is spent in exciting the residual nucleus, while a few hundred keV are available as kinetic energy for the neutron. This considerably increases the low-energy neutron yield softening the neutron spectrum. This situation was observed for the first time by Bonner and Butler [39]. More recently, neutron spectra for deuteron energies near 1 MeV were measured by Watterson et al. [40], confirming the previous results (Fig. 2).

In order to maximize the benefit of the population of the N6, N7 and N8 states, thin Be targets can be useful. For instance, in a 2 μm thick Be target, an incident deuteron with 1.1 MeV loses an energy of ~100 keV before leaving the Be layer. Under these conditions all reactions occur at an energy range that preferentially populates the excited states in ^{10}B, thus producing low energy neutrons, and eliminating all of the high energy neutrons produced by deuterons of energies lower than 1.0 MeV (which would be present in a thick target). In other words, the appropriate selection of the target thickness makes it possible to eliminate most of the highest-energy neutrons from the primary spectrum.

From a technological point of view, the ^{9}Be(d,n) reaction shows three key advantages over ^{7}Li(p,n) and ^{9}Be(p,n):

- As mentioned above, metallic Be is much more convenient than Li as a high-power target, due to the high melting point and thermal conductivity of Be.
- The threshold for ^{7}Li(p,n) and for ^{9}Be(p,n) are 1.88 and 2.06 MeV respectively. Then, the low deuteron energies involved in the ^{9}Be(d,n) reaction imply a significant advantage for the design and construction of an accelerator devoted to BNCT as far as voltage is concerned.
- Last but not least, there is no residual radioactivity in the ^{9}Be(d,n) case, while the ^{7}Be, 53 day radioactivity produced by the ^{7}Li(p,n) reaction is a non-negligible complication to deal with.

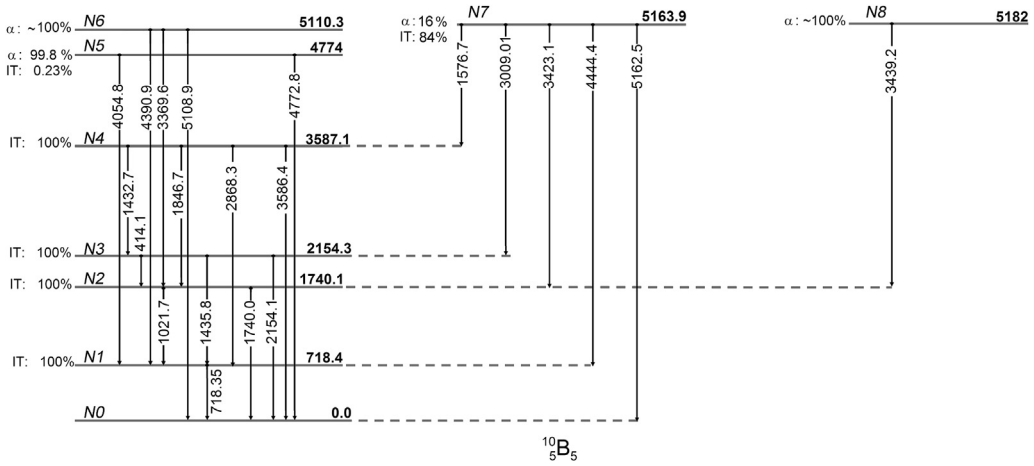

Figure 1. Level-scheme of ^{10}B with gamma emission (Data from Capote et al. [38]).

In this work, we evaluate the possibility of producing therapeutic neutron beams through a 30 mA current beam of low-energy deuterons and thin Be targets. The 30 mA beam current is the design value for the accelerator being developed in our laboratory [37]. This value is quite high but is believed to be within reach since there are currently several systems capable of producing the proton beam intensity and energy required by BNCT. The most notorious systems are the injectors for the large facilities like, e.g., the Oak Ridge Spallation Neutron Source (SNS) [41]. There are several types of ion sources able to produce proton beams of several tens of mA, both for negative [41] and positive ions (see Ref. [42] for the 200 mA source developed for the International Fusion Materials Irradiation Facility). These are frequently plasma volume sources excited through different processes like radiofrequency or filament driven plasma discharge sources [43]. This last one is the option we are following [37]. As far as accelerators are concerned, there are both electrostatic [44] as well as radiofrequency quadrupoles (ESQ and RFQ) machines. Our group, continuing the tradition initiated by Berkeley [23,24] is developing a Tandem electrostatic quadrupole system.

The thermal power left in the thin Be target is of the order of 15 kW and the total power carried by the beam is approximately 45 kW. This power can be safely carried away with efficient water cooling, taking into account that the melting temperature of Be is quite high. In this respect it is relevant to mention that even a metallic Li target can be kept solid by appropriate cooling [24,45] for power densities of up to 1 kW/cm^2. Some target designs are being tested in our group [46]. In these designs, the Be layer is deposited on a relatively thin slab (made of e.g., W or Mo), resistant to hydrogen and radiation damage, in which the deuterons stop. The deuterons emerge from the thin Be target with an energy of ~1 MeV. The Coulomb barrier for the deuterons on these materials is at least 5 MeV, thus suppressing completely any nuclear process. Finally the two layers are deposited on a Cu backing which provides the mechanical strength to separate the high vacuum from the cooling water and also gives a high conductivity medium to efficiently carry away the heat deposited by the beam.

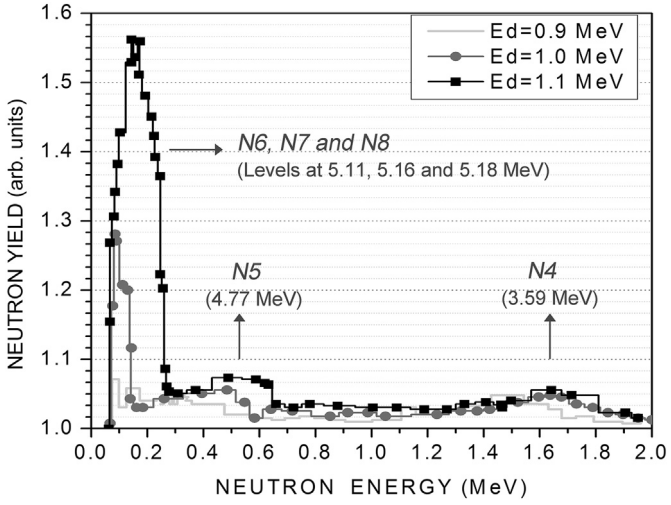

Figure 2. Neutron emission spectra (only 0–2 MeV shown) from Watterson et al. [40] for deuteron energies close to the threshold for excitation of the N6, N7 and N8 states and showing the relative intensity and growth of the low-energy component.

Preliminary results on the feasibility of ^{9}Be(*d*,*n*)-based neutron sources have already been published in a conference proceeding as a short communication [47]. Since then, major improvements were made in the BSA design and in the neutron source models. Concerning the BSA, the design we present here is more realistic for clinical use than our previous one. A conical collimator was added in order to facilitate patient positioning. Also, the flat beam port was replaced by an elliptical-shaped port, which resulted in much better dose performances. Concerning the neutron source models, a more realistic description of the angular distributions was introduced. In a realistic situation the hypothesis of isotropy (which was assumed for our previous models) is not correct since the low-energy region of the neutron spectrum is strongly forward peaked. This correction is introduced in this work, by means of a new source modeling method based on the Monte Carlo simulation of the emitted neutrons.

Finally, a deeper-going dose analysis compared to the previous one is presented here. In particular, a component analysis and a study of the dose due to gamma emissions from the residual nucleus are now included.

Materials and methods

Source modeling

To derive a closed mathematical form for the complete neutron spectrum it is necessary to know which is the process that produces the (*d*,*n*) reaction (i.e. transfer, compound nucleus formation, etc). This information can be derived from the shape of the differential cross section curves (with respect to the CM angle). For the N0 to

N4 states, the differential cross section does not show the characteristics of a unique process. Only the fourth excited state is formed as the result of a unique mechanism. In this case, a stripping mechanism can be identified. The shapes of the angular distributions of the other groups show that not only deuteron stripping and compound nucleus formation are involved, but also the interference of both processes. There are theoretical expressions for the stripping and compound nucleus cross sections [48–50] that fit well the experimental cross section curves. However, for the N5 to N8 excited states, there are no cross-section curves available in the literature for the energy range of our interest. For this reason, it is not possible to derive a closed mathematical form for the complete neutron spectrum. However, numerical models can be built following the procedure given below.

Consider a deuteron with an energy$E$ impinging on a very thin Be target. After the (d,n) reaction, the residual nucleus ^{10}B is left in the N-th excited level. The kinetic energy $E_n$of a neutron emitted is determined as:

$$E_n(\varepsilon_N) = \left[\frac{\sqrt{M_d M_n E}\cdot\cos(\theta) + \sqrt{M_d M_n E\cdot\cos^2(\theta) + (M_B + M_n)\cdot[M_B\cdot(Q-\varepsilon_N) + (M_B - M_d)\cdot E]}}{M_B + M_n}\right]^2 \quad (1)$$

where M_d, M_n and $M_B$are the mass of the deuteron, the neutron and the ^{10}B nucleus respectively, θ is the emission angle in the lab system,ε_N is the energy of the N-th excited state of ^{10}B, and Q = 4.36 MeV is the Q-value of the ^{9}Be(d,n)^{9}B reaction. It can be easily shown from Eq. (1) that, for a given excited state, the maximum and the minimum possible neutron energies (namely $E_n^{max}(\varepsilon_N)$ and $E_n^{min}(\varepsilon_N)$) correspond to the forward (θ=0°) and the backward (θ=180°) neutron emissions respectively. As shown in Fig. 1, there are nine possible final states in the residual nucleus ^{10}B (N0–N8) for deuterons near and above 1 MeV. Hence, there are nine different neutron structures (i.e. groups of neutrons produced by the population of any of the excited levels in the residual nucleus ^{10}B) in the complete neutron spectrum. The lower and upper edges of each neutron structure are $E_n^{min}(\varepsilon_N)$ and $E_n^{max}(\varepsilon_N)$ respectively.

For a thin target (not thin enough to neglect the energy loss), the energy spectrum (in units of neutrons per unit energy and charge) for each neutron structure is determined as:

$$\eta_i(E_n)|_{E,\Delta E} = \frac{N}{q}\cdot\frac{d\sigma_i(\overline{E})}{dE_n}\cdot\frac{1}{S(\overline{E})}\Delta E \quad (2)$$

where ΔE is the energy loss of deuterons in the target, $d\sigma_i/dE_n$ is the differential cross section for the i-th excited state, $S$is the stopping power of deuterons on Be. N is the number of Be atoms per unit volume, q is the charge of deuterons and $\overline{E}$ is a certain deuteron energy in the range $[E-\Delta E, E]$.

The complete neutron spectrum is then:

$$\eta(E_n)|_{E,\Delta E} = \sum_0^8 \eta_i(E_n)|_{E,\Delta E} \quad (3)$$

Eq. (2) is valid when the cross-section and the stopping power vary slowly in the $[E-\Delta E, E]$ interval. The stopping power is approximately constant over the $[E-\Delta E, E]$ range but it is not the case for the cross-section. As shown in Fig. 2, the low-energy neutron production increases rapidly for energies E near and above the threshold for the population of the N6, N7 and N8 excited levels. This suggests that the cross-section for this group of levels also increases rapidly, and therefore Eq. (4) should be used:

$$\eta_i(E_n)|_{E,\Delta E} = \frac{N}{q}\cdot\int_{E-\Delta E}^{E}\frac{d\sigma_i(E')}{dE_n}\cdot\frac{1}{S(E')}dE' \quad (4)$$

Note that Eq. (4) is also equivalent to the subtraction of the thick target spectra produced by deuterons with an initial energy of $E-\Delta E$ from the one produced by deuterons with an initial energy of$E$:

$$\eta_i(E_n)|_{E,\Delta E} = \eta_i(E_n)|_{E,E} - \eta_i(E_n)|_{E-\Delta E,E-\Delta E} \quad (5)$$

Numerical models of the thick target neutron spectra $\eta_i(E_n)|_{E,E}$ were built based on data available in the literature. For the neutron structures belonging to the N5-to N8 excited states, cross-section data $d\sigma_i(E)/dE_n$ are not available but experimental thick target neutron spectra $\eta_i(E_n)|_{E,E}$ are (experimental spectra with errors typically in the 5%–20% range) [40,51,52]. In most of these experimental spectra, the neutron structures associated with N0 to N4 excited levels are missing. For these structures, the cross-section data $d\sigma_i(E)/dE_n$ are available. For this reason, two different modeling methods were used, for the N0 to N4 and for the N5 to N8 excited states, depending on the availability of experimental data.

- The neutron associated with the N0 to N4 states were simulated from partial cross-section data as follows:
  1. The distance D traveled in the Be target by a deuteron without undergoing a (d,n) reaction was generated through a random procedure between from 0 to D_{MAX} (being D_{MAX} the range of deuterons in Be), which takes into account the energy dependence of the (d,n) cross-section.
  2. The deuteron energy E' at a depth D was calculated as:

$$E' = E - \int_0^D \frac{dE}{dx}\,dx \quad (6)$$

where E is the bombarding energy and dE/dx is the stopping power S of deuterons in Be.

  3. Then, the deuteron undergoes a (d,n) reaction at D. The final state of the residual nucleus is determined by the partial cross-section $\sigma_i(E')$ (i = 0,…, 4), which is proportional to the probability of undergoing a (d,n) reaction leaving the residual nucleus in the N_i excited state. Partial cross-sections were taken from Ref. [53].
  4. The neutron emission angle θ was determined as a random variable, with a distribution taken from Guzek et al. [54].
  5. The neutron energy is determined by the nuclear reaction kinematics.

- On the other hand, the neutron structures associated with the N5 to N8 excited states of ^{10}B were calculated by interpolation of the experimental spectra reported in the literature [40,51,52].

Finally, all the complete spectra were integrated over energy and angle to normalize them according to the total neutron yields given by Kononov et al. [55].

As an example, the neutron source modeled for $E = 1.4$ MeV and $\Delta E = 0.3$ MeV at different emission angles is shown in Fig. 3.

Compared to our previous source models [47], the models we present here constitute a more realistic representation of the neutron beams. In our previous work the angular distributions were considered as isotropic. In a realistic situation the hypothesis of isotropy is not entirely correct since the low-energy neutron structures are strongly forward peaked. This could be due to a strong contribution of the deuteron stripping process, where the proton is captured with $l_p = 0$ and/or $l_p = 1$ for neutrons leading to the N6–N7 and N8 excited states [56].

Beam shaping strategy

The first stage of beam shaping focused on softening the primary neutron spectra, through an appropriate choice of the bombarding energy and the target thickness. A possible estimator of the spectral hardness is the below-to-above 1 MeV neutron energy yield ratio:

$$R = \frac{Y_{<1\mathrm{MeV}}}{Y_{>1\mathrm{MeV}}} \tag{7}$$

Neutron yields above 1 MeV ($Y_{<1\mathrm{MeV}}$) were calculated by integrating the following expression over energy range of deuterons in the Be target:

$$Y_{>1\mathrm{MeV}} = \frac{N}{q}\int_{E_R}^{E}\frac{\sigma(E')}{S(E')}\,\mathrm{d}E' \tag{8}$$

where N is the number of Be atoms in the target, $\sigma(E')$ is the production cross-section for neutrons above 1 MeV as a function of the bombarding energy, $S(E') = \mathrm{d}E/\mathrm{d}x$ is the stopping power of deuterons in Be and q is the charge of deuterons. The upper integration limit E is the energy of the incident deuteron, and the lower integration limit E_R is the residual energy of the deuteron after leaving the target.

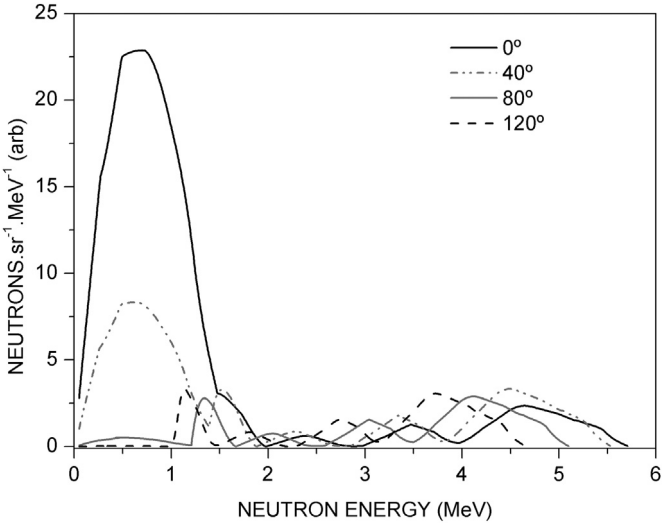

Figure 3. Neutron source modeled for a deuteron beam of $E = 1.4$ MeV and an energy loss in the target of $\Delta E = 0.3$ MeV at some different emission angles.

The cross-section $\sigma(E')$ curve was taken from Shpetnyi's data [53].

Neutron yields below 1 MeV ($Y_{<1\mathrm{MeV}}$) were calculated as:

$$Y_{<1\mathrm{MeV}} = Y - Y_{>1\mathrm{MeV}} \tag{9}$$

where Y is the total neutron yield. Total neutron yields were taken from Kononov et al. [55].

The parameter R was calculated for energy losses ranging from 50 to 450 keV in steps of 50 keV, as a function of the bombarding energy. Then, the bombarding energy was determined (for each thickness) as the one which resulted in the highest R. In this way, eight neutron sources (i.e. configurations of target thickness and bombarding energy) were selected as "candidates" for use in BNCT.

The second stage was focused in the epithermalization of these "candidate" neutron sources. For this purpose, a Beam Shaping Assembly (BSA) design was proposed (Fig. 4). The BSA consisted in a square cross-section moderating volume delimited by lead reflecting walls. The moderator volume was formed by successive layers of Al and AlF_3/Al. The volume AlF_3 and Al each material was chosen to mimic Fluental™ (69 w-% AlF3, 30 w-% Al and 1 w-% LiF), which was successfully used in nuclear reactor epithermal columns. We have eliminated LiF from our configurations because the neutron capture on Li strongly reduced the neutron flux at the beam port, increasing too much the treatment times.

A 5 cm-lead shield was added next to the production target in order to reduce dose due to gamma emissions from excited states of the residual nucleus ^{10}B. The whole BSA was covered with 4 cm thick natural Lithium Polyethylene (7.5% of Li by weight) as a neutron shielding material. A conical-shaped collimator was added in order to delimit the beam and to facilitate patient positioning. A 30 mA deuteron beam current was considered throughout.

Concerning the fast neutron shielding, Lithium Polyethylene has been successfully used for this purpose as in the nuclear power and nuclear medicine industry. Fast neutrons are slowed down (thermalized) by elastic scattering on hydrogen present in polyethylene. Then, thermal neutrons are absorbed by neutron capture on ^{6}Li through ^{6}Li$(n,\alpha)^3$H (natural lithium contains about 7.5w-% of this isotope); and on ^{1}H through ^{1}H$(n,\gamma)^2$H (radiative capture). The relative importance of neutron capture on ^{6}Li and ^{1}H can be roughly estimated by comparison of the macroscopic cross sections $\Sigma = \rho_A \times \sigma$ (ρ_A = atomic density of ^{6}Li or ^{1}H in the material; and σ = thermal neutron capture cross section for ^{6}Li$(n,\alpha)^3$H or ^{1}H$(n,\gamma)^2$H). Taking into account the material composition and tabulated cross-section data [57]:

$$\frac{\sum(\mathrm{Li})}{\sum(\mathrm{H})} = \frac{7.164\times10^{-4}\,\frac{\mathrm{atoms}}{\mathrm{cm.barn}}\times 940\ \mathrm{barn}}{7.652\times10^{-2}\,\frac{\mathrm{atoms}}{\mathrm{cm.barn}}\times 0.35\ \mathrm{barn}} = \frac{0.673\ \mathrm{cm}^{-1}}{0.027\ \mathrm{cm}^{-1}} \sim 25$$

Total dose rate evaluated on the lateral sides of the BSA is reduced to about 30%, compared to the BSA configuration without the lithium polyethylene shielding. Future work will focus on a further reduction of the dose in the lateral directions, in order to fulfill the radiation protection regulations. A BSA configuration installed within a wall can also be useful and we have not discarded it yet.

This new BSA design is a more realistic for clinical use than our previous design [47]. Apart from the conical collimator, the improved design beam port consists in an elliptical surface while the previous one was a flat port. These modifications derived in better dose performances, as will be pointed out in the Results section.

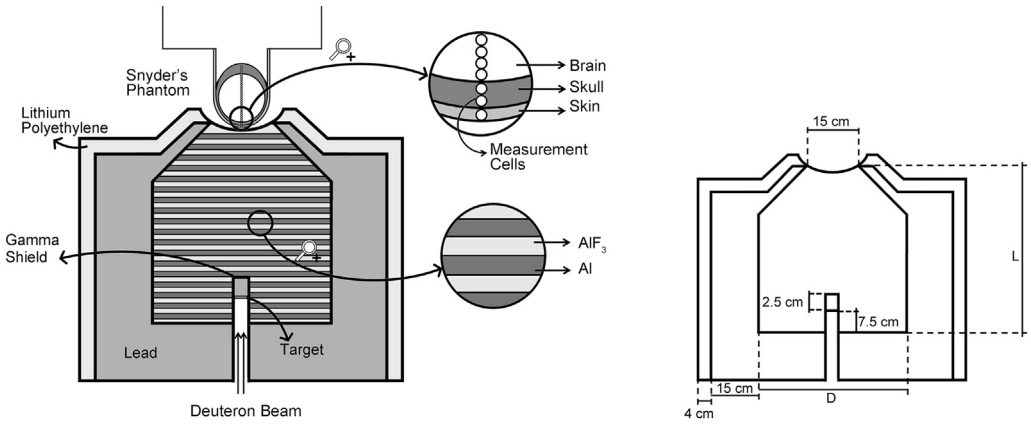

Figure 4. Beam Shaping Assembly design with a Snyder phantom (left) and the relevant dimensions considered for our Monte-Carlo study.

In order to obtain the best possible beam quality for each candidate source, an optimization of the BSA dimensions was performed. The optimized magnitudes in this study were the BSA length and the cross-section area. The other dimensions such as the thickness of lithium polyethylene and the lead walls were kept fixed. In this study, the outputs for BSA lengths of 20–60 cm and cross-sections ranging from 15 × 15 cm^2 to 50 × 50 cm^2 (Fig. 4) were simulated using the Monte Carlo N-particle code MCNP5 1.51 [58]. Depth dose profiles were recorded for each BSA configuration. From these, the BSA geometry was determined as the configuration that maximized the dose delivered to the tumor in a 60 min treatment, within the constraints imposed by healthy tissue dose adopted tolerance (radiobiological weighted doses of 11.0 and 16.7 Gy for healthy brain and skin respectively).

The strategy to reach the maximum dose value can be described as follows

First, a rectangular path was followed in the two-dimensional parameter space (length, cross-section). For a given starting value of the cross-section, we move in the direction of the length coordinate until the largest dose value is found. Subsequently, we fix that length value and move parallel to the cross-section axis until the maximum dose value is obtained. This cycle is repeated until it converges to a maximum dose value.

To simplify calculations a non-stopping target was considered in the simulations. As mentioned in the introduction, the Be target deposited on a water-cooled W (or Mo)/Cu backing must be implemented in a realistic situation, in order to carry away the power deposited by the deuteron beam. All these layers are quite thin (W less than 10 μm; Cu a few mm) and do not contribute to additional neutron production. Hence, the use of such a target will not affect the final characteristics of the epithermal neutron beam in any significant way. Furthermore, in a realistic target, the beam spot size (radius) should be larger than about 4 cm, if the total power carried by the beam is 45 kW (taking into account that power densities of up to 1 kW/cm^2 can be safely handled). To simplify MC simulations we considered a point-beam, since no differences in dose distributions were found between the simulated point-beam and the realistic one.

MCNP simulations

For dose calculations the F4 tally (volume average neutron/photon fluence) was used. Kerma factors [59] as a function of the neutron/photon energy were taken as the fluence-to-dose conversion coefficients, using the DE and DF cards.

The neutron source was coded in terms of coupled distributions, where the independent variable is the energy and the dependent variable is the emission angle. Energy values were coded as histograms (SI card, option H in MCNP) and emission angles were defined by the probability density (DS card, option A). Particle weights (WGT cards) were set as the total neutron yield, to obtain the tally results in Gy/mA-s units.

Dose and treatment time calculation

Snyder's head phantom [60] was considered and all tissue compositions were taken from the ICRU-46 report [61]. The doses were evaluated in spherical cells within the Snyder phantom, placed at different points along the center line in the head (through scalp, skull and brain) aligned with the beam port axis (Fig. 4).

Doses D were calculated as the radiobiological weighted sum of the boron dose D_B, thermal and fast neutron doses (D_{Ther} and D_{Fast}) and the gamma dose D_γ:

$$D = w_B D_B + w_{Ther} D_{Ther} + w_{Fast} D_{Fast} + w_\gamma D_\gamma \quad (10)$$

The first component is due to the boron thermal neutron capture $^{10}B(n,\alpha)^7Li$. D_{Ther} arises primarily from the thermal neutron capture on ^{14}N present in tissues, and D_{Fast} stems mainly from neutron elastic collisions on hydrogen, $^1H(n,n)^1H$. The last contribution (D_γ) primarily comes from neutron radiative capture on hydrogen atoms in tissues. The corresponding weighting factors w_i [62] are listed in Table 1. In this work all the expressed doses are radiobiological weighted unless otherwise indicated. The weighting factors for fast, thermal and gamma dose are called Relative Biological Effectiveness' (RBE's). For boron dose the weighting factor is called Compound Biological Effectiveness (CBE) since it not only depends on the radio-sensitivity of the tissue but also on the applied boron compound and its microdistribution.

A standard value of 15 μg/g [63] was adopted for the ^{10}B concentration in blood. ^{10}B concentrations in skin and tumor were assumed to be 1.5 and 3.5 times the concentration in blood respectively [64,65].

Table 1
Radiobiological weighting factors for each tissue.

	Weighting factor	Skin	Skull	Healthy brain	Brain tumor
CBE:	w_B	2.5	1.3	1.3	3.8
RBE's:	w_{Ther}	3.2	3.2	3.2	3.2
	w_{Fast}	3.2	3.2	3.2	3.2
	w_γ	1.0	1.0	1.0	1.0

The treatment time was determined as the minimum between the following three values: (a) the maximum allowed time, that is 60 min; (b) the time required to reach the dose limit for healthy brain (11.0 Gy) and (c) the time required to reach the dose limit for healthy skin (16.7 Gy).

Treatable depth (TD) and advantage depth (AD)

Depth dose profiles along the beam port central axis direction were evaluated in order to calculate treatable depth ranges and advantage depths. The treatable depth (TD) was determined as the region in brain where the total doses to tumor were ≥40 Gy. The advantage depth (AD) was determined as the maximum depth at which the tumor dose still exceeds the maximum healthy brain dose.

Dose due to gamma emissions from excited states of the residual nucleus ^{10}B

A detailed source model for these gamma emissions requires a detailed knowledge of the partial neutron yields Y_i for each excited state Ni of ^{10}B. This information can be obtained through the following expression:

$$Y_i = \frac{N}{q} \cdot \int_{E_R}^{E} \sigma_i(E') \cdot \left(\frac{dE'}{dx}\right)^{-1} dE' \quad (11)$$

where N is the number of relevant atoms in the target; $\sigma_i(E)$ is the neutron production partial cross-section for the Ni state of the residual nucleus ^{10}B as a function of the energy, dE/dx is the stopping power of the bombarding particle in the target material, q is the charge of the projectile, E and E_R are the bombarding and the residual energy of the deuteron respectively. Unfortunately, some of the partial cross-sections are not available in the literature. In spite of the lack of complete data about all the partial cross-sections, it is possible to calculate an upper bound for this dose component. This can be carried out by considering that the only state that is populated is the one that produces the highest gamma dose rate.

The cascade of gamma rays emitted from each excited state of ^{10}B in the decay to the ground state can be easily obtained from tabulated gamma emission probabilities taken from Capote et al. [38]. These data are given in Table 2. From excited states N1 to N4, the residual ^{10}B nucleus decays to the ground state 100% via gamma emission while from excited states N5 to N8, the $^{10}B^*$ nucleus decays mostly to the ground state of ^6Li via alpha emission. This is due to the fact that the threshold for alpha emission (i.e the threshold of the $^6Li + \alpha$ reaction) is about 4.46 MeV, which is slightly lower than the energy of the N5 excited level. From this data, numerical gamma source models were built and gamma dose rates were obtained by means of the MCNP5 1.51 code for the BSA configurations described in Section 2.2.

Dose and treatment time uncertainties

Uncertainties in dose calculation were calculated taking into account the following contributions:

i) Neutron spectra uncertainty. To calculate this contribution, a sample of 10 neutron spectra were randomly generated (for each "candidate" source) taking into account the uncertainty derived from the source modeling method. These neutron spectra were used as input data for 10 MCNP runs. Then, the uncertainty from the neutron spectra was calculated as the standard deviation (one sigma) of the results derived from the 10 MCNP runs (typically 2%).
ii) One-sigma statistical uncertainty given by MCNP outputs.

Hence, the total uncertainty is calculated as the square root of the sum of the squares of these two contributions.

Table 2
Adopted levels and emissions of ^{10}B. (Data from Capote et al. [38]).

Level	Level energy (keV)	J^π	$T_{1/2}$[a] or Γ[b]	Eγ (keV)	Pγ[c]	Multipolarity
N0	0.0	3+	Stable	…	…	…
N1	718.380	1+	$T_{1/2}$: 0.7070 ns			
			% IT[d] = 100	γ_{10}: 718.353	100	E2
N2	1740.05	0+	$T_{1/2}$: 4.9 fs	γ_{21}: 1021.7	100	M1
			% IT = 100	γ_{20}: 1740.0	<0.2	
N3	2154.27	1+	$T_{1/2}$: 1.48 ps	γ_{32}: 414.1	51.6	M1
			% IT = 100	γ_{31}: 1435.8	27.3	M1 + E2
				γ_{30}: 2154.1	21.1	E2
N4	3587.13	2+	$T_{1/2}$: 102 fs	γ_{43}: 1432.7	14	M1 + E2
			% IT = 100	γ_{42}: 1846.7	<0.3	
				γ_{41}: 2868.3	67	M1 + E2
				γ_{40}: 3586.4	19	M1 + E2
N5	4774.0	3+	Γ: 7.8 eV			
			% IT = 0.23	γ_{51}: 4054.8	99.5	E2
			% α[e] = 99.8	γ_{50}: 4772.8	0.5	M1 + E2
N6	5110.3	2-	Γ: 0.978 keV	γ_{62}: 3369.6	5	M2
			% IT = 3.3E-03	γ_{61}: 4390.9	31	E1
			% α ~ 100	γ_{60}: 5108.9	64	E1
N7	5163.9	2+	Γ: 1.79 eV	γ_{74}: 1576.7	7.8	M1
			% IT = 84	γ_{73}: 3009.1	65.3	M1
			% α = 16	γ_{72}: 3423.1	<0.5	E2
				γ_{71}: 4444.4	22.6	M1
				γ_{70}: 5162.5	4.4	M1 + E2
N8	5182	1+	Γ: 110 keV			
			% IT = 5.4E-5			
			% α ~ 100	γ_{82}: 3439.2	100	M1

[a] $T_{1/2}$ = half-lives of the level.
[b] Γ = level width %.
[c] Pγ = Probability that a level decays through the given gamma-ray emission. Pγ is the ratio of the total electromagnetic decay (gamma + internal conversion) of the level to the intensity of the gamma-ray.
[d] IT = % isomeric transition.
[e] % α = % alpha decay.

Results and discussion

Results from beam shaping: target-deuteron energy configurations

R vs. bombarding energy curves for different target thicknesses are shown in Fig. 5a, and the "candidate" neutron sources are listed in Table 3.

As the target thickness increases, the bombarding energy at the maximum *R* shifts to the higher energy region. This can be explained by the fact that the highest-energy neutron productions for all the target thicknesses show a local minimum (Fig. 5b). This is because the cross-sections for the lowest-energy levels of ^{10}B, N0 to N4, show a local minimum at about 1.2 MeV [50]. Since the total neutron production increases slightly with the bombarding energy, the maximum *R* is formed at the same bombarding energy that minimizes the highest-energy neutron production.

The fact that the maximum *R* value is higher for thinner targets is consistent with the increasing of the neutron spectrum average energy with the target thickness (Table 3).

As mentioned in the Introduction, the benefit of using a thin target results from the preferential population of the N6, N7 and N8 high-energy levels of ^{10}B in the low bombarding energy regime. The threshold for the population of these states (which produce the lowest energy neutrons) is about 0.9–1.0 MeV. When the residual

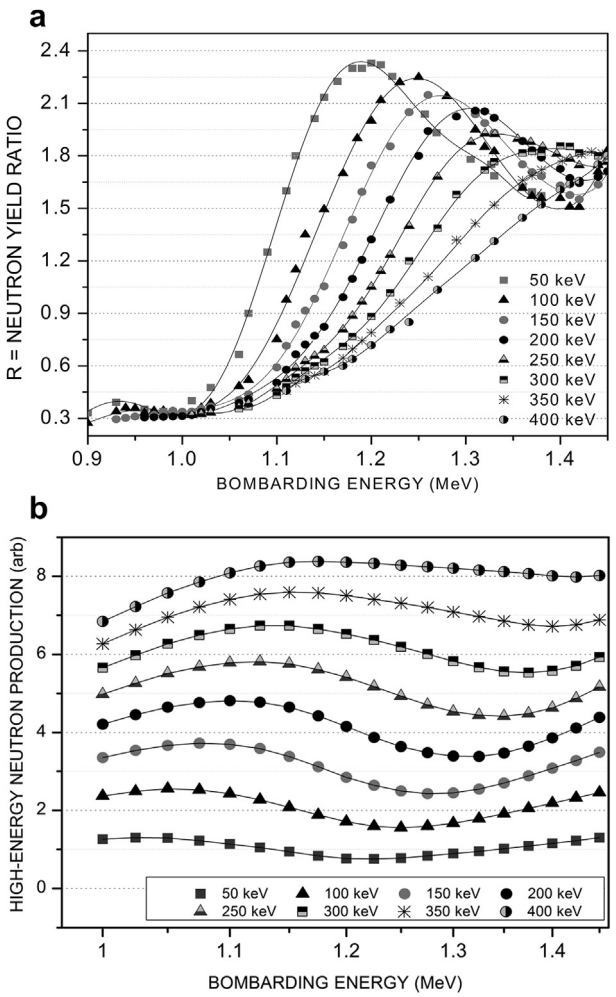

Figure 5. (a) Below-to-above 1 MeV neutron yield ratio R and (b) neutron production from the N0 to N4 excited states of ^{10}B, for thin targets as a function of deuteron energy. Each curve corresponds to a different deuteron energy loss in the target (i.e. to a different target thickness).

energy of the deuterons is higher than this threshold, it is energetically possible for *all* the (d,n) reactions to leave the residual nucleus in any of these levels. Since these are preferentially populated over the others, most of the reactions result in the emission of low energy neutrons. When the residual energy of deuterons is lower than the threshold, there are some reactions that leave the ^{10}B in the low-energy levels and hence produce only undesirable high-energy neutrons. Note that, in agreement with this, the residual energies for all the sources (#1–8) are slightly higher than the threshold.

Table 3
Target energy that maximizes the below-to-above 1 MeV neutron yield (R) for each target thickness. Also given is the total neutron yield.

Source ID	Energy loss (keV)	Bombarding energy (MeV)	Target thickness (μm)	Average energy (MeV)	R	Total neutron yield (neutron/mC)
#1	50	1.20	0.89	1.44	2.33 ± 0.60	3.83×10^{09}
#2	100	1.24	1.82	1.46	2.26 ± 0.29	2.45×10^{10}
#3	150	1.27	2.78	1.48	2.15 ± 0.19	4.49×10^{10}
#4	200	1.31	3.78	1.52	1.93 ± 0.13	6.61×10^{10}
#5	250	1.35	4.82	1.57	1.93 ± 0.10	8.75×10^{10}
#6	300	1.40	5.92	1.65	1.83 ± 0.08	1.12×10^{11}
#7	350	1.44	7.03	1.68	1.80 ± 0.07	1.39×10^{11}
#8	400	1.45	8.06	1.70	1.80 ± 0.05	1.62×10^{11}

In this way, as the bombarding energy increases, thicker targets are possible. However, increasing the deuteron energy implies necessarily an increasing of the neutron energy, regardless of the final state of the residual nucleus ^{10}B. For this reason, the maximum R value decreases and also the R vs. bombarding energy curves become flatter as the target thickness is increased.

Results from beam shaping: BSA geometry

Depth dose profiles for the optimal BSA configuration found for the "candidate sources" are shown in Fig. 6. These profiles showed that sources #4 to #8 resulted in acceptable doses deliverable to the tumor, without exceeding either the maximum treatment time (60 min) or the dose constraints for the healthy brain and skin.

The results in Table 4 show that treatable and advantage depths, and also the maximum dose deliverable to the tumor increase as the bombarding energy is increased, while the treatment time and the maximum doses to healthy tissues remain practically

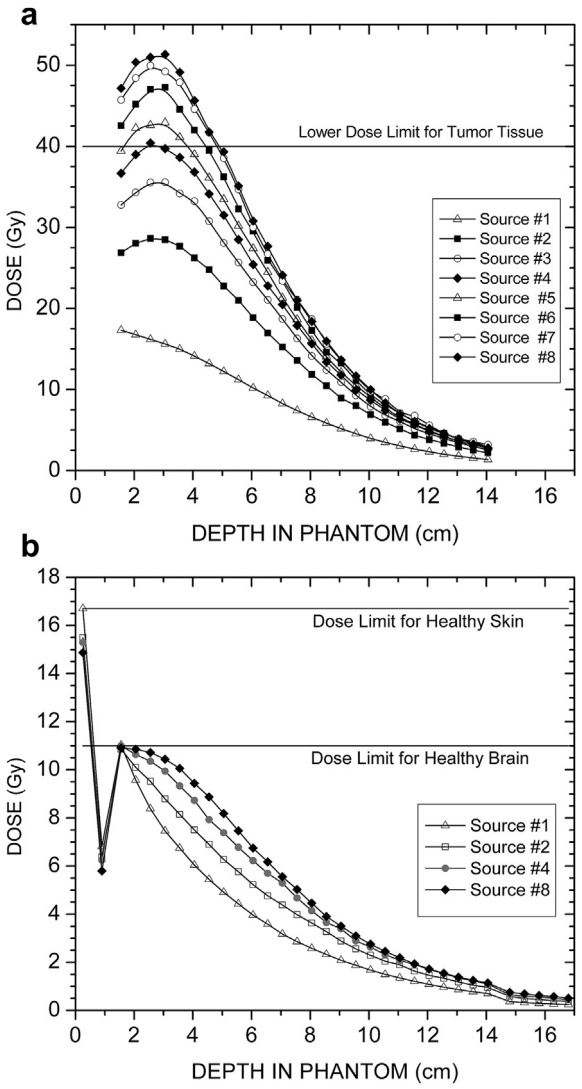

Figure 6. Simulated depth dose profiles (a) for brain tumor and (b) for healthy tissue obtained with the optimal BSA configurations. Healthy tissue dose profiles for sources #3 and #5 do not differ appreciably from the dose profile for source #4, as well as the ones for sources #6 and #7 do not differ from the one for source #8. The first point (at 0 cm in depth) and the last one (at 17 cm) correspond to skin, and the second point (at 0.9 cm) and the ones from 14.8 to 16.3 cm correspond to the skull where no boron is present.

Table 4
Doses, treatable depths and treatment times calculated for the proposed neutron sources. The optimized dimensions of the BSA are also shown. The MDT position, AD and TD ranges are referenced to the skin surface (brain tissue extends from 1.55 cm to 14 cm in depth relative to the skin surface).

Source ID	L[a] (cm)	A[b] (cm^2)	MDT[c] (Gy)	MDT Position (cm)	AD[d] (cm)	TD[e] (cm)	MHSD[f] (Gy)	MHBD[g] (Gy)	<DHB>[h] (Gy)	TT[i] (min.)
#1	21	35 × 35	16.9 ± 0.3	1.72	5.64	–	16.7 ± 0.4	10.7 ± 0.2	2.52 ± 0.05	58 ± 2
#2	34	35 × 35	28.6 ± 0.6	2.75	8.41	–	15.5 ± 0.4	10.8 ± 0.3	2.91 ± 0.06	60 ± 1
#3	39	41 × 41	35.6 ± 0.8	2.86	9.01	–	15.7 ± 0.4	11.0 ± 0.3	3.03 ± 0.09	59 ± 2
#4	43	41 × 41	40.4 ± 0.8	2.82	9.26	2.30–2.80	15.2 ± 0.4	11.0 ± 0.3	4.28 ± 0.09	58 ± 2
#5	47	39 × 39	42.9 ± 0.9	2.74	9.40	1.65–3.82	14.9 ± 0.4	11.0 ± 0.3	4.27 ± 0.09	60 ± 1
#6	49	40 × 40	47.3 ± 1.0	2.82	9.58	1.55–4.45	15.2 ± 0.4	11.0 ± 0.3	4.48 ± 0.09	57 ± 2
#7	52	39 × 39	50.0 ± 1.2	2.76	9.70	1.55–4.81	15.2 ± 0.5	11.0 ± 0.4	4.52 ± 0.09	58 ± 2
#8	55	40 × 40	51.3 ± 1.1	2.72	9.79	1.55–4.82	15.0 ± 0.4	10.9 ± 0.3	3.31 ± 0.08	60 ± 1

[a] L = Moderator Length.
[b] A = Moderator Cross-Section.
[c] MDT = Maximum Total Dose to Tumor.
[d] AD = Advantage Depth.
[e] TD = Treatable Depth.
[f] MHSD = Maximum Healthy Skin Dose.
[g] MHBD = Maximum Healthy Brain Dose.
[h] <DHB> = Mean Dose to Healthy Brain.
[i] TT = Treatment time.

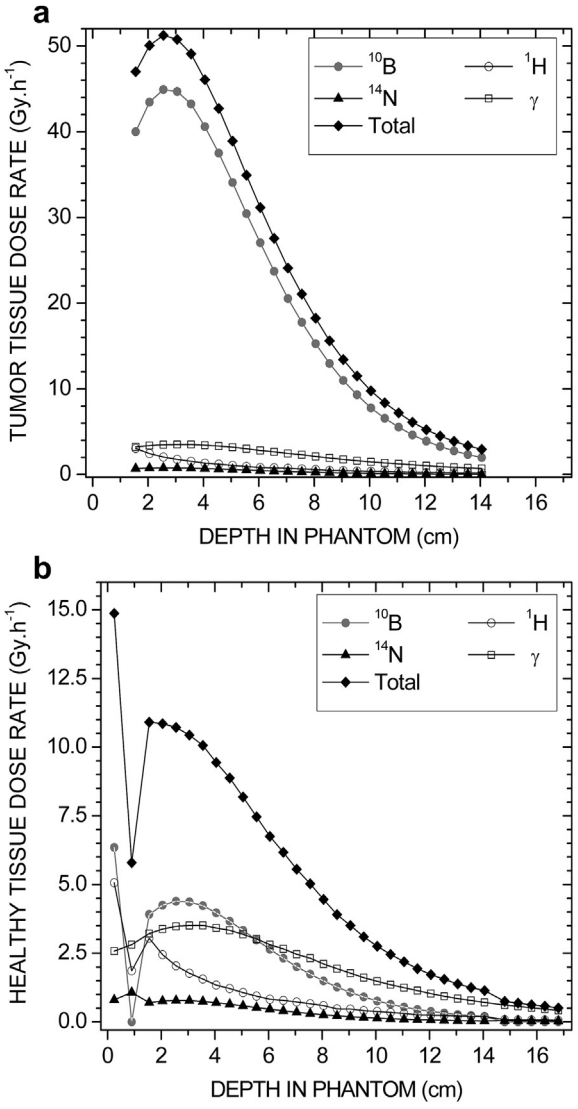

Figure 7. Depth dose profiles of the main contributions to tumor (a) and the healthy tissue (b). Jump discontinuities in the healthy tissue profiles are due to the different healthy tissues in Snyder's phantom (skin, skull, brain). The dip at ~1 cm corresponds to the skull and is due to the fact that there is no ^{10}B uptake in skull, and hence, the dose contribution from boron neutron capture is zero for this tissue.

unchanged. Therefore, sources #7 and #8 show the best dose performance, since larger treatable depths and higher doses to tumor are obtained by these sources. For the latter, the profiles of the main dose contributions are shown in Fig. 7.

Better dose performances were reached here compared to our previous results in Ref. [47], the maximum doses delivered to the

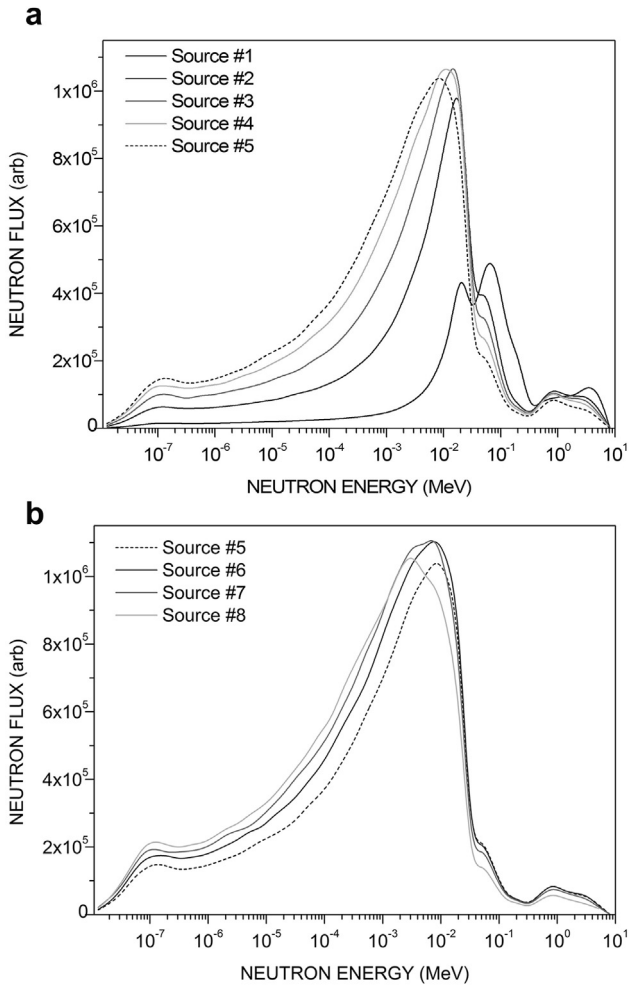

Figure 8. Neutron spectra at the beam port for sources #1 to #5 (a) and for sources #5 to #8 (b).

tumor were increased by about 15%. On the other hand, treatment times were reduced, since it was not possible for any source with our previous BSA design to deliver more than 40 Gy to the tumor in treatments shorter than 1 h.

For sources #1, #2 and #3 the total doses to tumor are lower than 40 Gy for any depth in brain and no treatable depths can be calculated. For these sources, there is a strong fast-neutron contribution to the neutron spectrum (Fig. 8) which would require larger moderators to efficiently moderate the primary neutron fluxes at expense of larger treatment times. Since the neutron yields for these sources are too low, it is not possible to increase the amount of moderating material without exceeding the treatment time limit (60 min), due to the loss of neutrons in the moderating volume.

By removing the treatment time constraint (and applying multiple-fraction-treatments), larger moderating volumes are feasible and it is possible to enhance the maximum dose to the tumor without increasing the doses delivered to healthy tissues. In this situation, the treatment time is determined as the minimum time to reach the healthy tissue dose limits (either 16 Gy for healthy skin or 11 Gy for healthy brain, whichever occurs first). Treatment times as a function of the moderator length are shown in Fig. 9 a and Fig. 9b shows the doses as a function of the treatment time for source #3. Without the treatment time constraint, the maximum dose deliverable to the tumor (MDT) increases as the moderator length (or the treatment time) is increased until it reaches a "plateau" regime, at about 58 Gy. This behavior is essentially the same for all the sources, but differs in the treatment times involved (due to the different neutron yields) (see Table 5). For all the BSA lengths in Fig. 9, the MHBD is 11 Gy, since the healthy brain dose limit is reached first. The MHSD does not show a significant change as the moderator length increases. The MHSD decreases from 15.7 Gy for the single-fraction treatment (Table 4) to 15.1 Gy and 14.5 Gy, for the double-fraction treatment and for the plateau regime respectively (Tables 5 and 6).

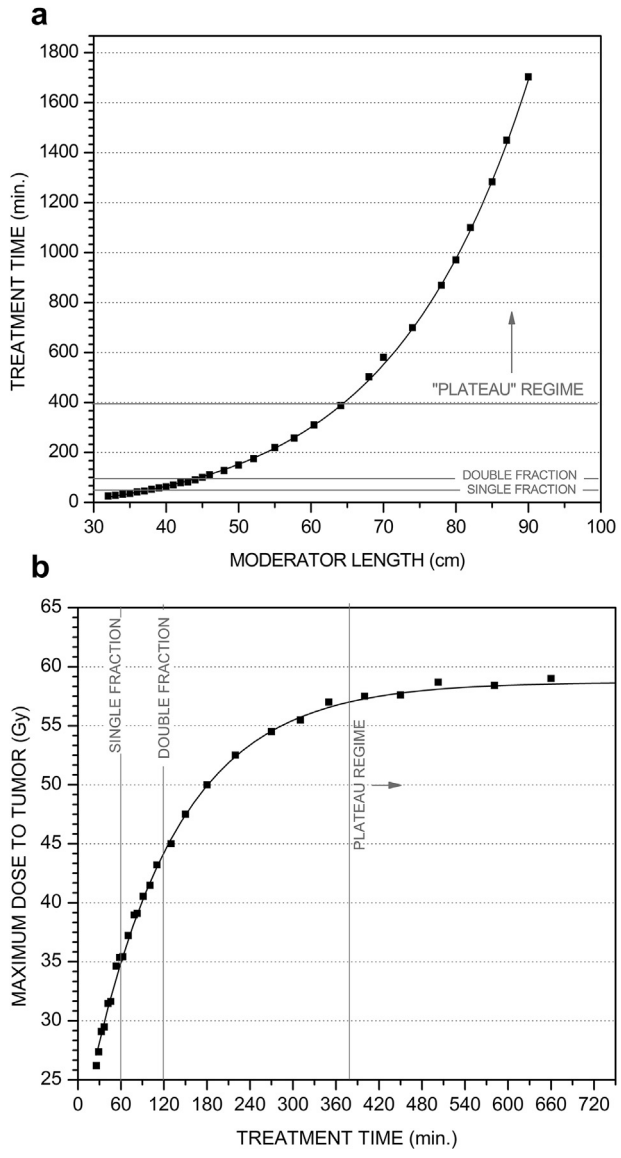

Figure 9. (a) Treatment time as a function of the moderator length obtained with source #3, (b) maximum dose to the tumor (MDT) as a function of the treatment time for the same neutron source. Increasing the moderator length from 39 (single-fraction treatment, 60 min) to 47 cm (double-fraction treatment, 120 min) allows reaching a MDT of 47.1 Gy. This makes the source #3 a viable source for the double-fraction configuration. Similar results were found for source #4.

Table 5
Maximum doses to tumor and healthy tissues in the "plateau" regime.

Source the ID regime	Moderator length (cm)	MDT (Gy)	MHBD (Gy)	MHSD (Gy)	Time to reach "plateau" (min)
#1	75	59.8 ± 1.5	11.0 ± 0.3	14.4 ± 0.4	>1000
#2	80	60.7 ± 1.4	11.0 ± 0.3	14.7 ± 0.4	>1000
#3	85	59.8 ± 1.5	11.0 ± 0.3	14.5 ± 0.4	>1000
#4	85	60.0 ± 1.5	11.0 ± 0.3	14.8 ± 0.4	776
#5	80	59.8 ± 1.3	11.0 ± 0.3	14.5 ± 0.4	467
#6	80	58.7 ± 1.2	11.0 ± 0.3	14.6 ± 0.4	356
#7	80	58.9 ± 1.3	11.0 ± 0.3	14.3 ± 0.3	284
#8	75	59.0 ± 1.2	11.0 ± 0.3	14.6 ± 0.4	150

Due to the long treatment times, it is impractical to work in the "plateau" regime. However, sources #6, #7 and #8 (i.e. the sources with highest neutron yield), allow us to work quite near the "plateau" if one is willing to split the treatment into 2 irradiations of 60 min each (Table 6). On the other hand, although MDT's are somewhat further into the "plateau regime", sources #3 and #4 become feasible, since the dose performances are still acceptable.

Fractionated BNCT schemes arise as a matter of interest, not only for the potential implementation of a ^{9}Be(d,n)-based source, but also for a ^{7}Li(p,n)-based one. For the latter, a fractionated scheme (and consequently longer treatment times) would make possible the use of lower beam currents, and therefore, most of the difficulties involved in target cooling would be significantly reduced. In the case of a ^{9}Be(d,n)-based source the use of high beam currents is not so critical concerning the target cooling requirements. In this case, the neutron yields (which are quite low) constitute the critical parameter that makes difficult to further reduce the treatment times. Independently of the neutron producing reaction, fractionated schemes would help the implementation of an accelerator-based BNCT facility, with all the benefits that an in-hospital facility entails. On the other hand, even larger beam currents in the Be case are conceivable and already exist [42].

Table 6
Maximum doses to tumor and healthy tissues delivered after 2 irradiations of 60 min each.

Source ID	Moderator length cm)	MDT (Gy)	MHSD (Gy)	MHBD (Gy)
#1	25.3	20.0 ± 0.5	16.3 ± 0.4	11.0 ± 0.2
#2	40.1	37.4 ± 0.8	15.5 ± 0.4	11.0 ± 0.2
#3	47.1	44.1 ± 1.0	15.1 ± 0.4	11.0 ± 0.2
#4	52.1	49.6 ± 1.2	15.0 ± 0.4	11.0 ± 0.2
#5	56.2	52.7 ± 1.2	14.8 ± 0.3	11.0 ± 0.2
#6	60.0	54.8 ± 1.2	14.8 ± 0.3	11.0 ± 0.2
#7	63.9	55.6 ± 1.2	14.2 ± 0.3	11.0 ± 0.2
#8	66.3	56.8 ± 1.2	14.7 ± 0.3	11.0 ± 0.2

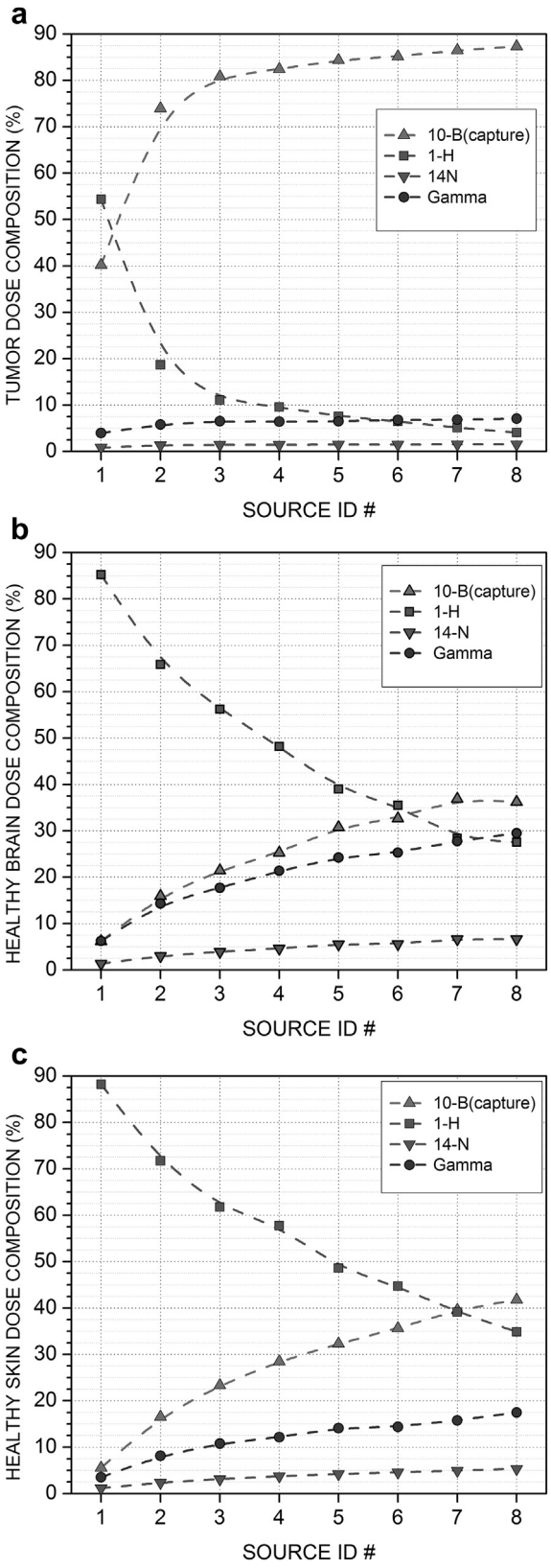

Figure 10. Main percentage contributions to the total biological weighted dose to tumor (a), healthy brain (b) and healthy skin (c). Main percentage contributions for healthy brain and tumor tissue were calculated at the depth of maximum total weighted dose.

It is important to emphasize that the therapeutic effectiveness of fractionated BNCT has already been demonstrated [66] in some cases. It was proven that fractionated (or "sequential") BNCT implies a significant enhancement of the tumor response without additional radiotoxicity effects in the precancerous tissue, compared to a single BNCT application. Moreover, fractionated schemes have already been implemented in the clinic [16,67,68].

BNCT dose component analysis

The different contributions to the total dose to tumor are shown in Fig. 10a. Except for source #1, the main contribution to the total dose in tumor is due to neutron capture in boron, as desired for BNCT. For source #1, the most important contribution (of about 54%) belongs to fast neutron scattering from hydrogen $^{1}H(n,n)$. For this source, the total neutron yield is too low (see Table 3), so a very short BSA length was obtained in order not to exceed the treatment time limit (60 min). As mentioned above, the amount of moderating material in the BSA is not enough to efficiently moderate the highest-energy neutrons. For sources #2 and #3, whose total neutron yields are still low, this dose contribution is still quite high (19% and 11% respectively). This is consistent with the fact that sources #1-#3 cannot provide an acceptable treatment.

For sources #6 to #8, the gamma dose is the most important of the non-specific contributions to tumor dose. This contribution includes the dose from all gamma rays produced by the interaction of neutrons in the patient's tissues (mainly via $^{1}H(n,\gamma)$ reaction) and in the BSA, but does not include gamma emissions from the target itself because of the excited states of the residual nucleus ^{10}B of the neutron producing reaction $^{9}Be(d,n)^{10}B$. Gamma dose from $^{9}Be(d,n)^{10}B^{*}$ is discussed in Section 3.4.

Concerning healthy brain the most important dose contribution is due to neutron scattering $^{1}H(n,n)$ for all the sources (Fig. 10b) except for sources #7 and #8, in which the main contribution belongs to ^{10}B dose. The main contribution to the total dose in skin belongs to fast neutron scattering from ^{1}H for all the sources except for sources #7 and #8, where neutron capture contributions becomes equally or more important (Fig. 10c). The $^{1}H(n,n)$ dose is essentially due to fast neutrons. Then, this dose contribution can be further reduced adding more moderating material to the BSA configuration, which implies splitting the treatment into 2 or more irradiations. A comparison between the $^{1}H(n,n)$ percentage dose contribution for a single and a double-fraction treatment is shown in Table 7.

Dose due to gamma emissions from excited states of the residual nucleus ^{10}B

As an example, dose rates in skin for source #8 are shown in Table 8. For this neutron source the upper bound for this dose

Table 7
Comparison of the $^{1}H(n,n)$ percentage contribution to total doses for a single-fraction of 60 min (SF) and for a double-fraction irradiation of 60 min each (DF).

Source ID	Tumor tissue		Healthy skin		Healthy brain	
	SF	DF	SF	DF	SF	DF
#1	54.3%	42.7%	88.2%	82.9%	85.5%	79.1%
#2	18.7%	17.6%	71.7%	60.1%	65.9%	53.8%
#3	11.1%	11.6%	61.7%	49.7%	56.2%	42.1%
#4	9.60%	7.38%	57.7%	38.0%	48.2%	33.0%
#5	7.57%	6.37%	48.6%	33.3%	39.0%	27.8%
#6	6.49%	4.18%	44.7%	26.2%	35.5%	19.7%
#7	5.11%	3.04%	39.1%	19.2%	28.4%	15.0%
#8	4.08%	2.83%	34.9%	19.8%	27.5%	14.0%

Table 8
Gamma emissions from each excited state of ^{10}B and their influence on the skin dose, for source #8. The state from which the dose rate is higher is in bold type. Uncertainties in doses and dose rates do not exceed 5%. Doses in skin were calculated assuming a 30 mA deuteron beam current and the treatment times listed in Table 2.

Excited state	<Eγ>[a] (MeV)	Eγ$_{min}$[b] (MeV)	Eγ$_{max}$[c] (MeV)	γ−rays per neutron	Dose rate in skin (mGy mA^{-1} h^{-1})	Dose in skin (mGy)
N1	0.718	0.718 (γ_{10})	0.718 (γ_{10})	1.00E+00	2.59E−02	0.78
N2	0.566	0.414 (γ_{32})	0.718 (γ_{10})	2.00E+00	1.13E−02	0.34
N3	0.934	0.414 (γ_{32})	2.154 (γ_{31})	2.31E+00	5.10E−01	15.3
N4	**1.800**	0.414 (γ_{32})	3.586 (γ_{40})	**1.99E+00**	**3.27E+00**	**98.0**
N5	2.392	0.718 (γ_{10})	4.773 (γ_{50})	4.59E−03	1.92E−02	0.58
N6	4.422	0.718 (γ_{10})	5.109 (γ_{60})	3.63E−05	~E−03	~1E−02
N7	1.771	0.414 (γ_{32})	5.163 (γ_{70})	2.37E+00	3.08E+00	92.3
N8	1.726	0.718 (γ_{10})	3.439 (γ_{82})	1.62E−06	~1E−05	~1E−04

[a] Average Energy of gamma rays.
[b] Minimum Energy of gamma rays.
[c] Maximum Energy of gamma rays.

Table 9
Upper bounds for skin and brain doses due to gamma emissions from excited states of the residual nucleus ^{10}B. The state from which the dose rate is higher is given in brackets. Total uncertainties in doses and dose rates do not exceed 6%. Maximum doses were calculated assuming a 30 mA deuteron beam and the treatment times listed in Table 4.

Source ID	Maximum γ dose rate in skin (mGy mA^{-1} h^{-1})	Maximum γ dose rate in brain (mGy mA^{-1} h^{-1})	Maximum γ dose in skin (mGy)	Maximum γ dose in brain (mGy)
#1	11.7 (N7)	9.18 (N7)	328	257
#2	5.71 (N7)	4.94 (N7)	171	148
#3	4.25 (N7)	3.82 (N7)	125	113
#4	3.36 (N7)	3.11 (N7)	97	90
#5	2.75 (N7)	2.60 (N7)	83	78
#6	2.94 (N7)	2.80 (N7)	84	80
#7	3.07 (N4)	2.87 (N7)	89	83
#8	3.27 (N4)	2.95 (N7)	98	88

component is given by gamma emissions from N4, since the gamma dose rate is higher for this state than for the others. Taking into account the treatment time listed in Table 4, the dose in skin due to gamma emissions from excited states of the residual nucleus ^{10}B is expected to be lower than 98 mGy assuming a 30 mA deuteron beam. The corresponding results for all the neutron sources (#1 to #8), both for skin and brain tissues are listed in Table 9.

For sources #4 to #8 this dose component does not imply a significant increase of healthy tissue doses, since their values do not exceed the uncertainties associated to the BNCT doses listed in Table 4.

Conclusions

Eight neutron sources produced through the ^{9}Be(d,n)^{10}B reaction were evaluated as epithermal neutron sources for brain tumor BNCT treatments. These neutron sources were found by selecting the combinations of bombarding energy and target thickness that minimized the highest-energy neutron contribution to the primary neutron spectra.

Our Monte Carlo study has shown that good dose performances can be obtained by means of ~5-to-8 μm thick Be targets bombarded with deuterons from 1.35 to 1.45 MeV (i.e. sources #5 to #8) in a 60 min irradiation treatment. Using these neutron sources and considering a 30 mA deuteron beam, biological weighted doses from 40 to 51 Gy can be delivered to brain tumors of up to 4.8 cm in depth without exceeding the adopted dose limits for healthy skin (16.7 Gy) and healthy brain (11 Gy). For bombarding energies lower than 1.35 MeV and beryllium targets thinner than ~5 micron (i.e. sources #1 to #4), less-than 60-min-treatments are not feasible, since the total neutron yield is in these cases too low.

Fractionated treatments become of interest not only for a ^{9}Be(d,n)-based source but also for a ^{7}Li(p,n)-based one. For the latter, fractionation would allow the use of a less intense beam, and hence, to reduce most of the problems related to cooling requirements of a lithium target. In the case of a Be target, these requirements are less critical but the low neutron yields of the ^{9}Be(d,n) reaction make it difficult to reduce the treatment time below 1 h (which clearly can be compensated by higher beam currents). From the point of view of neutronics, the performances obtained with sources #5 to #8 can still be improved by removing the treatment time constraint and splitting the treatment into two 1-h sessions. Under this condition, the fast neutron contribution to the neutron spectrum is reduced; since longer BSA lengths are feasible. Assuming a two-irradiation treatment of 60 min each, doses delivered to tumor are increased by ~10% without affecting the doses delivered to healthy brain and skin. In addition, in a double-fraction configuration, thinner targets and lower bombarding energies (sources #3 and #4) become feasible.

It is important to point out that published work on “sequential” BNCT [66] demonstrated the therapeutic effectiveness of fractionated treatments.

The technological advantages of ^{9}Be(d,n)-based BNCT must be emphasized. First, the low bombarding energies involved in the ^{9}Be(d,n)^{10}B reaction (about half of the proton energy required for ^{7}Li(p,n)) imply a significant advantage for the design and construction of an accelerator devoted to AB-BNCT as far as voltage is concerned. Moreover, the thermal and mechanical superiority of a metallic Be target as compared to a Li one, together with the absence of residual radioactivity, mean very important benefits in terms of target engineering design and overall safety of the facility. Finally, even if we have chosen 30 mA's as the beam intensity goal, there is no special “barrier” at that value and there are already ion sources capable of producing more intense ion beams [42].

References

[1] Locher GL. Biological effects and therapeutic possibilities of neutrons. Am J Roentgenol Radium Ther Nucl Med 1936;36:1–13.
[2] Wazer DE, Zamenhof RG, Harling OK, Madoc-Jones H. Boron neutron capture therapy. In: Mauch P, Loeffler J, editors. Radiation oncology: technology and biology 1994. Saunders, Philadelphia.
[3] Special Issue: 14th International conference on neutron capture therapy. In: Kreiner AJ, et al., editors. Applied radiation and isotopes, vol. 36. Elsevier, Amterdam; 2010. p. 1631–940.
[4] Farr LE, Sweet WH, Robertson JS, Foster CG, Locksley HB, Sutherland DL, et al. Neutron capture therapy with boron in the treatment of glioblastoma multiforme. Amer J Roentgenol 1954;71:279–91.
[5] Sweet WH. Early history of development of boron neutron capture therapy of tumors. J Neuro-Oncol 1997;33:19–26.
[6] Soloway AH, Hatanaka H, Davis MA. Penetration of brain and brain tumor. VII. Tumor-binding sulfhydryl boron compounds. J Med Chem 1967;10:714–7.
[7] Snyder HR, Reedy AJ, Lennarz WJ. Synthesis of aromatic boronic acids, aldehydo boronic acids and a boronic acid analog of tyrosine. J Am Chem Soc 1958;80:835–8.
[8] Riley KJ, Binns PJ, Harling OK. A state-of-the-art epithermal neutron irradiation facility for neutron capture therapy. Phys Med Biol 2004;49:3725–35.

[9] Sauerwein W, Moss R, Wittig A, editors. Research and development in neutron capture therapy. Bologna (Italy): Monduzzi Editore S.p.A., International Proceedings Division; 2002.

[10] Savolainen S, Kortesniemi M, Timonen M, Reijonen V, Kuusela L, Uusi-Simola J, et al. Boron neutron capture therapy (BNCT) in Finland: technological and physical prospects after 20 years of experiences. Physica Med Eur J Med Phys 2013;29:233–48.

[11] Henriksson R, Capala J, Michanek A, Lindahl S, Salford LG, Franzén L, et al. Boron neutron capture therapy (BNCT) for glioblastoma multiforme: a phase II study evaluating a prolonged high-dose of boronophenylalanine (BPA). Radiother Oncol 2008;88:183–91.

[12] Busse PM, Harling OK, Palmer MR, Kiger 3rd WS, Kaplan J, Kaplan I, et al. A critical examination of the results from the Harvard-MIT NCT program phase I clinical trial of neutron capture therapy for intracranial disease. J Neurooncol 2003;62:111–21.

[13] Miyatake S, Tamura Y, Kawabata S, Iida K, Kuroiwa T, Ono K. Boron neutron capture therapy for malignant tumors related to meningiomas. Neurosurgery 2007;61:82–90.

[14] Barth RF, Vicente MGH, Harling OK, Kiger WS, Riley KJ, J Binns PJ, et al. Current status of boron neutron capture therapy of high grade gliomas and recurrent head and neck cancer. Radiat Oncol 2012;7:146–67. and cited references.

[15] Yamamoto T, Nakai K, Nariai T, Kumada H, Okumura T, Mizumoto M, et al. The status of Tsukuba BNCT trial: BPA-based boron neutron capture therapy combined with X-ray irradiation. Appl Radiat Isot 2011;69:1817–8.

[16] Kankaanranta L, Seppälä T, Koivunoro H, Saarilahti K, Atula T, Collan J, et al. Boron neutron capture therapy in the treatment of locally recurred head-and-neck cancer: final analysis of a phase I/II trial. Int J Radiat Oncol Biol Phys 2012;82:67–75.

[17] Wang LW, Wang SJ, Chu PY, Ho CY, Jiang SH, Liu YW, et al. BNCT for locally recurrent head and neck cancer: preliminary clinical experience from a phase I/II trial at Tsing Hua open-pool reactor. Appl Radiat Isot 2011;69:1803–6.

[18] Menéndez PR, Roth BMC, Pereira MD, Casal MR, González SJ, Feld DB, et al. BNCT for skin melanoma in extremities: updated Argentine clinical results. Appl Radiat Isot 2009;67:S50–3.

[19] Blue JW, Roberts WK, Blue TE, Gahbauer RA, Vincent JS. A study of low energy proton accelerators for neutron capture therapy. In: Hatanaka H (Niigata: Nishimura, editor). Neutron Capture Therapy, 1986. Proceedings of the Second International Symposium on Neutron Capture Therapy, Tokyo, Japan, October 1985, 147–58.

[20] Brownell GL, Kirsch JE, Kehayias J. Accelerator production of epithermal neutrons for neutron capture therapy. In: Hatanaka H (Niigata: Nishimura, editor). Neutron Capture Therapy, 1986. Proceedings of the Second International Symposium on Neutron Capture Therapy, Tokyo, Japan, October 1985, 127–38.

[21] Wu T, Brugger R, Kunze J. Low energy accelerator-based neutron source for neutron capture therapy. In: Barth R, Soloway A, editors. Advances in neutron capture therapy. New York: Plenum Press; 1993. p. 105–10.

[22] Kwan JW, Anderson OA, Reginato LL, Vella MC, Yu SS. A 2.5 MeV electrostatic quadrupole DC accelerator for BNCT application. Nucl Instrum Methods Phys Res B 1995;99:710–2.

[23] Kwan JW, Henestroza E, Peters C, Reginato LL, Yu SS. Design of a DC ESQ accelerator for BNCT application. In: Proceedings of the 14th International Conference on the Application of Accelerators in Research and Industry, Denton Texas, November, 1996, AIP Press, New York, 1997, vol. II, 1313–5; and references therein.

[24] Ludewigt BA, Bleuel DL, Chu WT, Donahue RJ, Kwan J, Reginat LL, et al. Development of an accelerator-based BNCT facility at the Berkeley Lab (Technical Report LBNL-416, Lawrence Berkeley National Laboratory, Berkeley, California, 1998. Available online URL: http//:www.osti.gov/bridge/servlets/purl/760281-TOdWOA/webviewable/.

[25] Blue TE, Yanch JC. Accelerator-based epithermal neutron sources for boron neutron capture therapy of brain tumors. J Neurooncol 2003;62:19–31. and cited references.

[26] Bisceglie E, Colangelo P, Colonna N, Paticchio V, Santorelli P, Variale V. Production of epithermal neutron beams for BNCT. Nucl Instrum Meth Phys Res A 2002;476:123–6.

[27] Burlon AA, Kreiner AJ, White S, Blackburn BW, Gierga DP, Yanch JC. In-phantom dosimetry using the $^{13}C(d, n)^{14}N$ reaction for BNCT. Med Phys 2001;28:796–803.

[28] Wang CK, Moore BR. Thick beryllium target as an epithermal neutron source for neutron capture therapy. Med Phys 1994;21:1633–8.

[29] Herrera MS, González SJ, Minsky DM, Kreiner AJ. Evaluation of performance of an accelerator-based BNCT facility for the treatment of different tumor targets. Physica Med Eur J Med Phys 2013;29(5):436–46.

[30] Halfon S, Paul M, Arenshtam A, Berkovits D, Bisyakoev M, Eliyahu I, et al. High-power liquid lithium target prototype for accelerator-based boron neutron capture therapy. Appl Radiat Isot 2011;69:1654–6.

[31] Kobayashi T, Miura K, Hayashizaki N, Aritomi M. Development of liquid-lithium film jet flow for the target of the $^{7}Li(p, n)^{7}Be$ reactions for BNCT. In: Proceedings of the 15th international congress on neutron capture therapy, p.112.

[32] Mitsumoto T, Yajima S, Tsutsui H, Ogasawara T, Fujita K, Tanaka H, et al. Cyclotron-based neutron source for BNCT. New challenges in neutron capture therapy. In: Proceedings of the 14th international congress on neutron capture therapy 2010. p. 519–22.

[33] Imoto M, Tanaka H, Fujita K, Mitsumoto T, Ono K, Maruhashi A, et al. Evaluation for activity of component of cyclotron-based epithermal neutron source (C-BENS) and the surface of concrete wall in irradiation room. Appl Radiat Isot 2011;69:1646–8.

[34] Yoshioka M, Matsumura A, Kumada H, Sakurai Y, Kiyanagi Y, Hiraga F, et al. Development of an accelerator based BNCT facility in Ibaraki. In: 15th International Congress on Neutron Capture Therapy. Tsukuba, Japan 2012.

[35] Mc Michael GE, Yule TJ, Zhou X-L. The Argonne ACWL, a potential accelerator-based neutron source for BNCT. Nucl Instrum Meth B 1995;99:847–50.

[36] Colonna N, Beaulieu L, Phair L, Wozniak GJ, Moretto LG, Chu WT, et al. Measurements of low-energy (d, n) reactions for BNCT. Med Phys 1999;26:793–8.

[37] Kreiner AJ, Castell W, Di Paolo H, Baldo M, Bergueiro J, Burlon AA, et al. Development of a tandem-electrostatic-quadrupole facility for accelerator-based boron neutron capture therapy. Appl Radiat Isotope 2011;69:1672–5. and cited references.

[38] Capote R, Herman M, Obložinský P, Young PG, Goriely S, Belgya T, et al. RIPL – reference input parameter library for calculation of nuclear reactions and nuclear data evaluations. Nucl Data Sheets 2009;110:3107–214.

[39] Bonner TW, Butler JW. Neutron thresholds from the reactions $T^{3}(p, n)He^{3}$, $Li^{7}(p, n)Be^{7}$, $Be^{9}(d, n)^{*}B^{10}$ and $O^{16}(d, n)F^{17}$. Phys Rev 1953;83:1091–6.

[40] Watterson JIW, Lanza RC, Guzek J, Tapper UAS, McMurray WR, Iverson E. The small deuteron accelerator as a source of slow neutrons. In: 5th Intern. Conf. on Applications of Nuclear Techniques, Crete, 1996; Proc. SPIE 1977:2867; 533–6.

[41] Welton RF, Stockli MP, Murray SN, Crisp D, Carmichael J, Goulding RH, et al. Next generation H-ion sources for the SNS. AIP Conf. Proc. 2009:1097; 181–90.

[42] Hollinger R, Volk K, Klein H. Measurement of the beam emittance of the Frankfurt proton source. Rev Sc Instrum 2002;73:1027–9.

[43] Stockli MP. CERN Accelerator School on Ion Sources, http://cas.web.cern.ch/cas/Slovakia-2012/Lectures/Stockli.pdf.

[44] Bieniosek FM, Celata CM, Henestroza E, Kwan JW, Prost L, Seidl PA, et al. 2-MV electrostatic quadrupole injector for heavy-ion fusion. Phys Rev ST Accel Beams 2005;8:010101.

[45] Bayanov B, Belov V, Kindyuk V, Oparin E, Taskaev S. Lithium neutron producing target for BINP accelerator-based neutron source. Appl Radiat Isot 2004;61:817–21.

[46] Gagetti L, Suarez Anzorena M, del Grosso MF, Kreiner AJ. Blancos de producción e neutrones para aplicaciones médicas y nucleares. presented at the 97° Reunión Nacional de Física, Villa Carlos Paz, Argentina, September 25–28, 2012.

[47] Capoulat ME, Minsky DM, Kreiner AJ. Applicability of the $^{9}Be(d, n)^{10}B$ reaction to AB-BNCT skin and deep tumor treatments. Appl Radiat Isot 2011;69:1684–7.

[48] Bathia AB, Huang K, Huby R, Newns C. Angular distribution in (d, p) and (d, n) reactions. Phil Mag 1952;43:485–500.

[49] Grant IP. Theory of (d, p) and (d, n) reactions I: general theory ignoring Coulomb effects. Proc Phys Soc A 1954;67:981–9.

[50] Grant IP. Theory of (d,p) and (d,n) reactions II: Coulomb corrections and numerical results. Proc Phys Soc A 1955;68:244–56.

[51] Whittlestone S. Neutron energy spectra from the thick target $^{9}Be(d, n)^{10}B$ reaction. AAEC/AE 399. Australian Atomic Energy Commission Research Establishment Lucas Heights, Australia 1976.

[52] Whittlestone S. Neutron distributions from the deuteron bombardment of a thick beryllium target. J Phys D: Appl Phys 1977;10:1715–23.

[53] Shpetnyi AI. Energy and angular distribution of neutrons emitted in the $Be^{9}(d, n)Be^{10}$ reaction. Soviet Phys JETP 1957;5:357–64.

[54] Guzek J, Tapper UAS, McMurray WR, Watterson JIW. Characterization of $^{9}Be(d, n)^{10}Be$ reaction as a source of neutrons employing commercially available radio frequency quadruopole (RFQ) linacs. In: 5th Intern. Conf. on Applications of Nuclear Techniques, Crete, Proc. SPIE 1997:286; 509–12.

[55] Kononov VN, Bokhovko MV, Kononov OE, Soloviev NA, Chu WT, Nigg D. Accelerator-based fast neutron sources for neutron therapy. Nucl Instrum Methods Phys Res A 2006;564:525–31.

[56] Riley PJ, Braben DW, Neilson GC. The 5.11 and 5.16 MeV levels of ^{10}B. Nucl Phys 1963;47:150–6.

[57] Lawrence Berkeley National Laboratory. LBNL Isotopes Project: Thermal Neutron Capture. http://ie.lbl.gov/ng.html.

[58] Brown F, Barret R, Booth T, Bull JS, Cox LJ, Forster RA, et al. MCNP Version 5. LA-UR-02–3935, Los Alamos National Laboratory, USA 2002.

[59] Chadwick MB, Barshal HH, Caswell RS, DeLuca PM, Hale GM, Jones DT, et al. A consistent set of neutron kerma coefficients from thermal to 150 MeV for biologically important materials. Med Phys 1999;26:974–91.

[60] Goorley JT, Kiger WS, Zamenhof RG. Reference dosimetry calculations for neutron capture therapy with comparison of analytical and voxel models. Med Phys 2002;29:145–56.

[61] International Commission on Radiation Units and Measurements. ICRU-report 46: photon, electron, proton and neutron interaction data for body tissues. Bethesda, Md., U.S.A 1992.

[62] Chadha M, Capala J, Coderre JA, Elowitz EH, Iwai J, Joel DD, et al. Boron neutron-capture therapy (BNCT) for glioblastoma multiforme (GBM) using the epithermal neutron beam at the Brookhaven National laboratory. Int J Radiat Oncol Biol Phys 1998;40:829–34.

[63] Kiger III WS, Lu XQ, Harling OK, Riley KJ, Binns PJ, Kaplan J, et al. Preliminary treatment planning and dosimetry for a clinical trial of neutron capture

therapy using a fission converter epithermal neutron beam. Appl Radiat Isot 2004;61:1075–81.
[64] Fukuda H, Hiratsuka J, Honda C, Kobayashi T, Yoshino K, Karashima H, et al. Boron neutron capture therapy of malignant melanoma using ^{10}B-para-boronophenylalanine with special reference to evaluation of radiation dose and damage to the normal skin. Radiat Res 1994;138:435–42.
[65] Coderre JA, Chanana AD, Joel DD, Elowitz EH, Micca PL, Nawrocky MM, et al. Biodistribution of boronophenylalanine in patients with Glioblastoma Multiforme: boron concentration correlates with tumor cellularity. Radiat Res 1998;149:163–70.
[66] Molinari AJ, Pozzi ECC, Monti Hughes A, Heber EM, Garabalino MA, Thorp SI, et al. "Sequential" boron neutron capture therapy (BNCT): a novel approach to BNCT for the treatment of oral cancer in the hamster cheek pouch model. Radiat Res 2011;175:463–72.
[67] Capala J, Stenstam BH, Sköld PM, Munck af Rosenschöld P, Giusti V, Persson C, et al. Boron neutron capture therapy for glioblastoma multiforme: clinical studies in Sweden. J Neurooncol 2003;62:135.
[68] Joensuu H, Kankaanranta L, Seppälä T, Auterinen I, Kallio M, Kulvik M, et al. Boron neutron capture therapy of brain tumors: clinical trials at the finnish facility using boronophenylalanine. J Neurooncol 2003;62:123–34.